



# Tuning oxygen vacancy in SnO<sub>2</sub> inhibits Pt migration and agglomeration towards high-performing fuel cells

Shenzhou Li<sup>a</sup>, Junyi Liu<sup>b</sup>, Jiashun Liang<sup>a</sup>, Zijie Lin<sup>a</sup>, Xuan Liu<sup>a</sup>, Yuan Chen<sup>c</sup>, Gang Lu<sup>b</sup>,  
Chengliang Wang<sup>c</sup>, Peng Wei<sup>a</sup>, Jiantao Han<sup>a</sup>, Yunhui Huang<sup>a</sup>, Gang Wu<sup>d</sup>, Qing Li<sup>a,\*</sup>

<sup>a</sup> State Key Laboratory of Material Processing and Die & Mould Technology, School of Materials Science and Engineering, Huazhong University of Science and Technology, Wuhan 430074, China

<sup>b</sup> Department of Physics and Astronomy California State University Northridge, Northridge, CA 91330, USA

<sup>c</sup> School of Optical and Electronic Information, Wuhan National Laboratory for Optoelectronics, Huazhong University of Science and Technology, Wuhan 430074, China

<sup>d</sup> Department of Chemical and Biological Engineering, University at Buffalo, The State University of New York, Buffalo, NY 14260, USA

## ARTICLE INFO

### Keywords:

Fuel cells  
Oxygen reduction reaction  
Durability  
Metal-support bonding interaction  
Electrocatalysis

## ABSTRACT

The serious durability concerns of carbon supported Pt electrocatalysts for oxygen reduction reaction (ORR) have strictly limited the commercialization of fuel cells. Herein, cable-like carbon nanotubes (CNTs)@SnO<sub>2</sub> core-shell supports with regulable electronic metal-support interaction (EMSI) are designed for Pt nanoparticles (NPs) as ORR catalysts. Impressively, the best-performing Pt-CNT@SnO<sub>2</sub> catalyst with optimized *d*-band center achieves an excellent activity (mass activity (MA) of 0.68 A mg<sub>Pt</sub><sup>-1</sup> at 0.9 V<sub>IR-free</sub> and peak power density of 1618 mW cm<sup>-2</sup>) and record-high durability in H<sub>2</sub>-O<sub>2</sub> fuel cells (9.2 % MA and 8 % power density loss after 5k cycles under 1.0–1.5 V) among the reported Pt-based catalysts, which is also superior to the U.S. DOE 2025 targets. Density functional theory (DFT) calculations reveal that the strong metal-support bonding interaction (SMSBI) endows much larger adhesion energy and migration barrier towards Pt atoms compared to carbon supports, leading to the extraordinarily high stability in fuel cells.

## 1. Introduction

Proton exchange membrane fuel cells (PEMFCs) with high energy conversion efficiency are considered as the promising sustainable power sources for vehicles and stationary applications [1,2]. The sluggish kinetics of oxygen reduction reaction (ORR) which happens at the cathode of a PEMFC requires significant amounts of Pt-based catalysts [3,4]. However, in the strongly oxidative and acidic conditions of a PEMFC, commercial Pt/C catalysts always suffer from severe performance degradation (>60 % activity loss after 30,000 voltage cycles, U.S. DOE 2025 target <30 %) due to the poor stability of carbon support and weak Pt-support interaction, leading to carbon corrosion, Pt dissolution, and agglomeration/detachment of Pt nanoparticles (NPs) [5–7]. More seriously, under fuel cell start-stop or load-change conditions, the cathode local potential will rise to as high as 1.5 V vs. reversible hydrogen electrode (RHE) and cause the rapid corrosion of carbon support (the standard potential of carbon oxidation reaction is 0.207 V vs. standard hydrogen electrode, SHE) [8,9]. Previous stability studies have revealed that the 1000 start-stop cycles of a PEMFC would result in ~35 % overall

porosity loss of the carbon supports [10].

So far, various alternative catalyst supports have been developed to improve the stability of ORR catalysts at high-potentials and oxidative environments, including the highly graphitized carbon [11,12], metal carbides [13–15], nitrides [16–18], etc. Besides, metal oxides with excellent stability in harsh environments (pH < 1, 0–1.5 V) based on Pourbaix diagram has attracted considerable attention as alternative catalyst supports, such as SnO<sub>2</sub> [19], TiO<sub>2</sub> [20,21], ZrO<sub>2</sub> [22]. Among them, Sn has a suitable ionic potential and strong M–O bond energy, which makes SnO<sub>2</sub> promising as a stable catalyst support (Fig. S1–S2) [23]. However, the low electron-conductivity of metal oxides (<10<sup>-5</sup> S cm<sup>-1</sup>) prevents them from being used as viable catalyst supports. Therefore, coating the conductive materials with metal oxides has been explored as a feasible means to prepare composite supports, but it is still challenging to balance the conductivity and anti-corrosion ability [24, 25]. On the other hand, the oxide supports can further affect the activity and stability of the catalysts via the metal-support interactions. For instance, antimony-doped SnO<sub>2</sub> as the support for Pt NPs is reported to be able to shift the *d*-band center of Pt via the electronic metal-support

\* Corresponding author.

E-mail address: [qing.li@hust.edu.cn](mailto:qing.li@hust.edu.cn) (Q. Li).

<https://doi.org/10.1016/j.apcatb.2022.122017>

Received 22 July 2022; Received in revised form 11 September 2022; Accepted 22 September 2022

Available online 24 September 2022

0926-3373/© 2022 Elsevier B.V. All rights reserved.

interaction (EMSI) with enhanced ORR activity [26]. In addition, theoretical calculations manifest that the strong metal-support bonding interaction (SMSBI), especially the adhesion energy between metals and various supports (e.g., carbides and oxides), could significantly impact the onset temperature of metal NP sintering [27]. However, tuning SMSBI on oxide supported noble-metal NPs towards ORR stability enhancement under high potential conditions are still far less explored. Hence, designing advanced anti-corrosive supports for Pt NPs and optimizing the metal-support interactions is highly desirable to prepare ORR catalysts with both high activity and durability.

In this paper, cable-like carbon nanotubes (CNTs)@SnO<sub>2</sub> core@shell structures are developed as an advanced support for Pt NPs towards high-performance ORR catalysis in PEMFCs. The presence of a small amount of CNTs (~ 20 wt%) ensure the electron-conductivity of the support while SnO<sub>2</sub> can effectively protect CNTs from corrosion in the harsh environment of a PEMFC. Meanwhile, the EMSI between SnO<sub>2</sub> and Pt NPs, which can be regulated by the concentration of oxygen vacancy in SnO<sub>2</sub>, could properly reduce the *d*-band center of Pt and optimize the ORR activity. Compared to commercial Pt/C and Pt-CNT, our Pt-CNT@SnO<sub>2</sub> catalysts exhibit much enhanced ORR activity and durability in both electrochemical half-cells and membrane electrodes assembly (MEA). More importantly, Pt-CNT@SnO<sub>2</sub> demonstrates the best stability among Pt-based ORR catalysts ever reported so far under high potential regions (1.0–1.6 V), with a much-reduced CO<sub>2</sub> yield at 1.6 V relative to Pt-CNT (10 vs. 80 ppm CO<sub>2</sub> mgC<sup>-1</sup>). Density functional theory (DFT) calculations suggest that the SMSBI between SnO<sub>2</sub> and Pt induce higher adhesion energy and migration barrier of Pt compared to conventional carbon, preventing the Pt particles from agglomeration.

## 2. Methods

### 2.1. Preparation of catalysts

Synthesis of CNT@SnO<sub>2</sub>-T: 10 mg CNTs were dissolved in 40 mL hydrochloric acid with pH = 1 for ultrasonic dispersion for half an hour. Then 1 g of anhydrous SnCl<sub>2</sub> was added and sealed the with polyethylene film. The reaction was performed at 60 °C for 3 h, and then centrifuged with deionized water and ethanol. Collecting the samples and dried with a freeze dryer. Then the samples were heat treated in air at a certain temperature (T = 0, 200, 300, 400, 500 °C), and the products were named as CNT@SnO<sub>2</sub>-T.

Synthesis of Pt-CNT@SnO<sub>2</sub>-T: 16 mg as-prepared CNT@SnO<sub>2</sub>-T was dispersed in a mixture of ethylene glycol and water, and 1 mL of 10 mg mL<sup>-1</sup> chloroplatinic acid solution was added to the mixture. Finally, the ratio of ethylene glycol to water was controlled to 3:1. The material was stirred and reflow at 130 °C for 1 h. The final catalyst Pt-CNT@SnO<sub>2</sub>-T was obtained by centrifugation and freeze drying.

Synthesis of Pt-CNT: 16 mg CNTs was dispersed in a mixture of ethylene glycol and water, and 1 mL of 10 mg mL<sup>-1</sup> chloroplatinic acid solution was added to the mixture. Finally, the ratio of ethylene glycol to water was controlled to 3:1. The material was stirred and reflow at 130 °C for 1 h. The final catalyst Pt-CNT@SnO<sub>2</sub>-T was obtained by centrifugation and freeze drying.

### 2.2. Electrochemical measurements

Electrochemical measurements were performed with 3-electrode system on CHI760e electrochemical workstation (Shanghai Chenhua Instrument Corporation, China). Glassy carbon rotating disk electrode was used as a working electrode (5 mm in diameter), Ag/AgCl (saturated KCl) as a reference electrode and platinum plate as a counter electrode. All potentials were experimentally converted to values with reference to a reversible hydrogen electrode (vs. RHE).

Pt-C, Pt-CNT and Pt-CNT@SnO<sub>2</sub>-T were dispersed in a mixture containing water, isopropanol and Nafion (5 %) (v/v/v = 1:1:0.1) to form a 2 mg mL<sup>-1</sup> ink. Ink was cast on the glassy carbon and dried under

ambient condition. The final loading of the Pt was kept at about 20 μg<sub>Pt</sub> cm<sup>-2</sup> (determined by ICP-MS).

The CV measurements were performed in N<sub>2</sub>-saturated 0.1 M HClO<sub>4</sub> solutions at a scan rate of 50 mV s<sup>-1</sup>. The ORR measurements were performed in O<sub>2</sub>-saturated 0.1 M HClO<sub>4</sub> using a rotating disk electrode (RDE) at a rotation rate of 1600 rpm and a sweep rate of 10 mV s<sup>-1</sup>, with iR-correction. Accelerate durability test was performed at room temperature by applying cyclic sweeps between 1.0 and 1.6 V (vs. RHE) in N<sub>2</sub>-saturated 0.1 M HClO<sub>4</sub> at a sweep rate of 200 mV s<sup>-1</sup>.

### 2.3. MEA preparation and fuel cell testing

Catalysts were mixed with Nafion®, n-propanol, and water by ultrasonication for 1 h to form homogeneous ink. The ink was then sprayed onto Nafion® 211 membrane at 70 °C. Fuel cell testing was performed in a single cell using a commercial fuel cell test system (Scribner 850e, Hephas Energy Corporation). The MEA was sandwiched between two graphite plates with single serpentine flow channels. The cell was operated at 80 °C with a backpressure of 150 kPa. Pure hydrogen and air/oxygen, with 100 % relative humidity (RH), were supplied to the anode at a gas flow rate of 200 sccm and cathode at a gas flow rate of 500 sccm. Fuel cell polarization curves were recorded using potential step mode with 50 mV/point (holding 2 min for each point). The ADT was performed at 80 °C by applying cyclic sweeps between 1.0 and 1.5 V in H<sub>2</sub>-N<sub>2</sub> at a sweep rate of 500 mV s<sup>-1</sup>.

### 2.4. Physicochemical characterizations

TEM images were taken from a FEI Tecani G2 20 with an operation voltage of 200 kV. HRTEM images were taken from a FEI Tecani G2 F30 with an operation voltage of 300 kV. The HAADF-STEM characterization was conducted on a JEOL JEMARM200F STEM/TEM with a guaranteed resolution of 0.08 nm. XRD were collected from Rigaku MiniFlex 600 diffractometer with a Cu radiation source (λ = 0.15406 nm). XPS spectra were collected from AXIS-ULTRA DLD-600 W. ICP-MS result was carried out from ELAN DRC-e. Extended X-ray absorption fine structure spectroscopy (EXAFS) at the Pt L<sub>3</sub>-edge was performed at BL11B of Shanghai Synchrotron Radiation Facility. The electron-storage ring was operated at 8 GeV with a current of 100 mA. A Si (111) double-crystal monochromator was employed. All XAS spectra were recorded at room temperature in transmission mode. EPR spectra were acquired on a Bruker EMXplus spectrometer.

### 2.5. DFT calculations

The density functional theory (DFT) calculations were performed using the Vienna ab initio simulation package (VASP) [28] based on the projector augmented-wave method [29]. The valence electron wave functions are expanded in the plane-wave basis sets with a kinetic energy cutoff of 400 eV. The electronic exchange-correlation functional is in the Perdew–Burke–Ernzerhof (PBE) form [30] with generalized gradient approximations. Based on the convergence test, the K-points sampling in the Brillouin zone employs the Monkhorst-Pack scheme [31] with a grid density of 2π × 0.02 Å<sup>-1</sup>. The conjugated gradient method is adopted to optimize the atomic structures, and convergence criteria of the total energy and the forces are set as 1 × 10<sup>-4</sup> eV and 0.01 eV Å<sup>-1</sup>, respectively. The diffusion barriers for a Pt atom on different surfaces are calculated based on the climbing image-nudged elastic band (CI-NEB) [32,33] method implemented in the VASP transition state tools, and the convergence criterion of the force is set to be 0.02 eV Å<sup>-1</sup>. The semiempirical DFT-D2 method [34] is adopted to account for the van der Waals (vdW) interaction. As shown in the Fig. S12, all the interface models are constructed with negligible lattice mismatch (<1 %), and a vacuum slab of 10 Å along the z-direction is used to minimize spurious interactions from the periodic images. The interfacial cohesive energy (*E*<sub>inter</sub>) is calculated as:

$$E_{\text{inter}} = -(E_{M/S} - E_M - E_S) / A_{\text{inter}}$$

where  $E_M$ ,  $E_S$  and  $E_{M/S}$  are the total energies of the metal slab ( $M$ ), the support slab ( $S$ ) and the combined metal and support ( $M/S$ );  $A_{\text{inter}}$  is interface area.

The migration barrier ( $E_b$ ) of a Pt atom is calculates as:

$$E_b = E_{TS} - E_{IS}$$

where  $E_{TS}$  is the energy of the transition state configuration at the saddle point and  $E_{IS}$  is the energy of the initial state configuration.

### 3. Results and discussion

#### 3.1. Structural characterizations

Cable-like CNT@SnO<sub>2</sub> were prepared by a wet-chemical approach followed by air annealing (Fig. 1a). Firstly, Sn<sup>2+</sup> precursor was nucleated and oxidized into SnO<sub>2</sub> at the carbonyl group on the surface of CNTs and grew up to completely cover its surface. Then CNT@SnO<sub>2</sub> was annealed in air from 200 to 500 °C to enhance the crystallinity and regulate the oxygen vacancy concentration of SnO<sub>2</sub>, and the sample were named as CNT@SnO<sub>2</sub>-T (T = annealing temperature). Finally, an ethylene glycol reduction method was used to load Pt NPs onto the CNT@SnO<sub>2</sub>. The similar method was used to prepare Pt-CNT as a

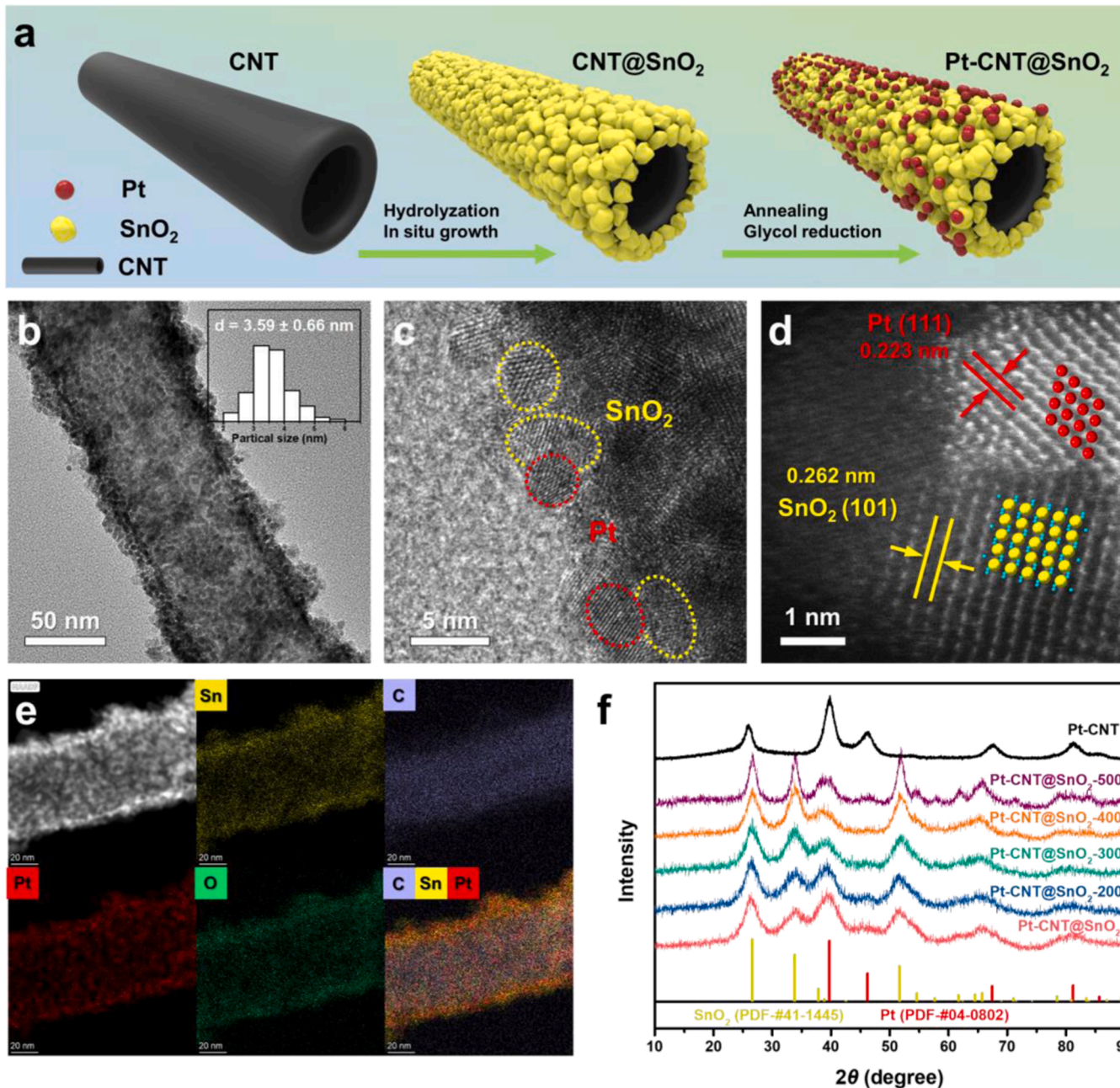


**Fig. 1.** (a) Schematic illustration of the synthetic route to Pt-CNT@SnO<sub>2</sub>-T. (b) HRTEM image of the Pt-CNT@SnO<sub>2</sub>-400. Inset: statistical distribution of particle size. (c) HRTEM image of the Pt-CNT@SnO<sub>2</sub>-400. Inset: the structure of SnO<sub>2</sub> and Pt, the red, yellow and blue balls represent Pt, Sn and O atoms, respectively. (d) HAADF-STEM image of Pt-CNT@SnO<sub>2</sub>-400. Inset: the structure of SnO<sub>2</sub> and Pt, the red, yellow and blue balls represent Pt, Sn and O atoms, respectively. (e) Elemental mappings of Pt, Sn, O and C of Pt-CNT@SnO<sub>2</sub>-400. (f) XRD patterns of the Pt-CNT and Pt-CNT@SnO<sub>2</sub> samples.



comparison. The mass loadings of Pt in Pt-CNT and Pt-CNT@SnO<sub>2</sub>-T are 15.6 % and 10 %, respectively, as measured by inductively coupled plasma optical emission spectrometer (ICP-OES).

The high-resolution transmission electron microscopy (HR-TEM) image of Pt-CNT@SnO<sub>2</sub>-400 is presented in Fig. 1b–c. Pt NPs are uniformly anchored on the surface of tubular CNT@SnO<sub>2</sub> structures, while the internal CNTs cannot be directly observed. The average size of Pt NPs was ca. 3.59 nm with a narrow size distribution. Other Pt-CNT@SnO<sub>2</sub> samples reveal similar core@shell structures and Pt particle sizes (Fig. S3). At the edge of catalysts, the observed lattice fringes can be identified as face centered cubic (fcc) Pt and rutile phase SnO<sub>2</sub>. It should be noted that crystalline SnO<sub>2</sub> particles are tightly stacked

around CNTs and the surface of CNT@SnO<sub>2</sub> is rugged. Fig. 1d is high-angle annular dark field scanning transmission electron microscopy (HAADF-STEM) image of Pt-CNT@SnO<sub>2</sub>-400, and the inter-plane spacings of 0.262 nm and 0.223 nm correspond to the (101) facet of SnO<sub>2</sub> and the (111) facet of Pt, respectively. Meanwhile, obvious interfaces can be observed between Pt and SnO<sub>2</sub> NPs, which is beneficial to the electron transfer between them. According to the elemental mapping results (Fig. 1e), the cable-like structure of CNT@SnO<sub>2</sub> can be obviously distinguished, while the width of internal CNTs is ~40 nm and the thickness of external SnO<sub>2</sub> layer is ~10 nm. The thermogravimetric test of CNT@SnO<sub>2</sub> (Fig. S4) shows that the mass ratio of SnO<sub>2</sub>/carbon is 4/1, which is higher than most previous researches [35–38] where the

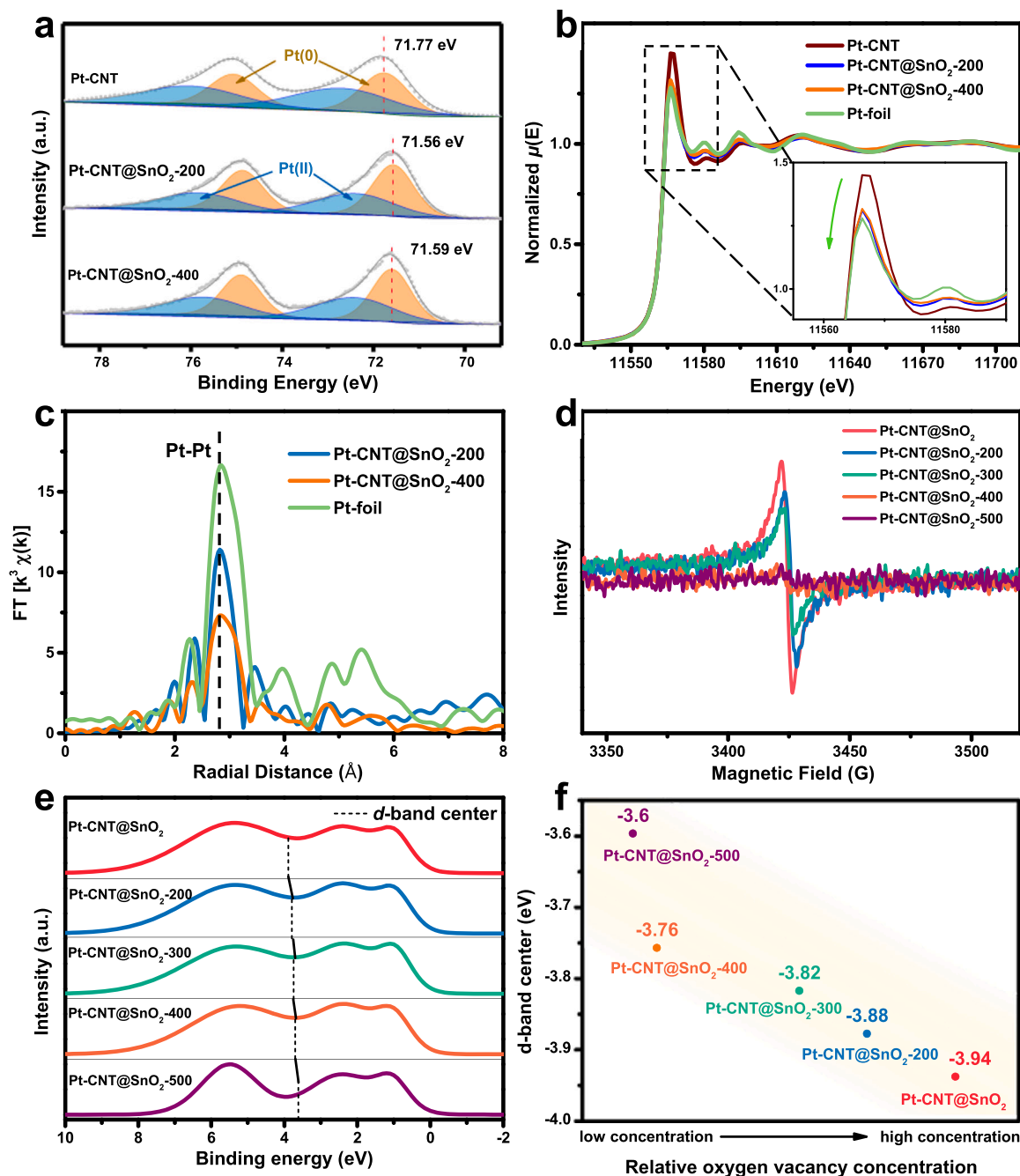


**Fig. 2.** (a) High-resolution Pt 4f XPS spectra of Pt-CNT, Pt-CNT@SnO<sub>2</sub>-200 and Pt-CNT@SnO<sub>2</sub>-400. (b) Pt L<sub>3</sub>-edge XANES spectra of Pt foil, Pt-CNT, Pt-CNT@SnO<sub>2</sub>-200 and Pt-CNT@SnO<sub>2</sub>-400. (c) Pt L<sub>3</sub> k<sup>3</sup>-weighted FT-EXAFS spectra of Pt foil, Pt-CNT@SnO<sub>2</sub>-200 and Pt-CNT@SnO<sub>2</sub>-400. (d) EPR spectra of Pt-CNT@SnO<sub>2</sub>. (e) Valence band XPS spectra of Pt-CNT@SnO<sub>2</sub>. The position of the d-band center is indicated by the black dotted line. (f) The relationship between d-band center of Pt and the relative oxygen vacancy concentration of SnO<sub>2</sub>.

carbon/oxide ratios are usually larger than 60 % and a large portion of Pt NPs are inevitably loaded on carbons. Such catalyst configuration will still suffer from Pt dissolution and migration in case of carbon corrosion. As a comparison, in our study, CNTs is tightly wrapped by SnO<sub>2</sub> and barely contact with Pt NPs. Noteworthy, SnO<sub>2</sub> not only protects the internal CNTs against corrosion in the harsh environments but also prevents the migration and agglomeration of Pt NPs loaded outside.

Fig. 1f shows the X-ray diffraction (XRD) patterns of the Pt-CNT and Pt-CNT@SnO<sub>2</sub> samples. The diffraction peaks at 25.9° of Pt-CNT is belonging to the graphitized CNTs. All of Pt-CNT@SnO<sub>2</sub> reveal the characteristic peaks of the rutile structure of SnO<sub>2</sub> (space group *P42/mnm*, JCPDS PDF #41-1445) and fcc structure Pt (space group *Fm-3m*, JCPDS PDF #04-0802), and the peak of CNT is too small to be identified. With the raise of the annealing temperature of CNT@SnO<sub>2</sub>, the peak position of SnO<sub>2</sub> have no shift and the diffraction peaks at 26.6°, 33.9°, and 51.8° correspond to the (110), (101), and (211) facets of SnO<sub>2</sub>, respectively. When the temperature rises to 500 °C, the diffraction peak of SnO<sub>2</sub> becomes steeper, indicating the particle sintering. TEM image proves that the cable structure of Pt-CNT@SnO<sub>2</sub>-500 collapses partly, likely due to the partial oxidation of CNTs at the elevated temperature (Fig. S4). In addition, the conductivity of the CNT@SnO<sub>2</sub> supports was measured by a four-probe method (Fig. S5). With the increase of annealing temperature, the conductivity of CNT@SnO<sub>2</sub> shows a volcanic relationship and reaches the highest value at 400 °C. Lower annealing temperature causes the poor crystallinity of SnO<sub>2</sub> and higher annealing temperature would lead to the oxidation of CNTs.

### 3.2. Electronic metal-support interaction

The Pt 4f X-ray photoelectron spectroscopy (XPS) spectra of the Pt-CNT@SnO<sub>2</sub> and Pt-CNT samples are depicted in Fig. 2a and Fig. S6, and all of Pt exhibits Pt(0) and Pt(II) states. The binding energy of Pt(0) 4f<sub>7/2</sub> for Pt-CNT, Pt-CNT@SnO<sub>2</sub>-200 and Pt-CNT@SnO<sub>2</sub>-400 are at 71.8 eV, 71.54 eV and 71.58 eV, respectively. Moreover, the Pt(0)/Pt(II) ratio of Pt-CNT is only 45 %, lower than that of Pt-CNT@SnO<sub>2</sub>-200 (56.8 %) and Pt-CNT@SnO<sub>2</sub>-400 (54.3 %). The negative shift of the Pt 4f binding energy and the increase of Pt(0)/Pt(II) ratio for Pt-CNT@SnO<sub>2</sub> compared to that of Pt-CNT point to the electron transfer from SnO<sub>2</sub> to Pt, resulting in a decrease in Pt valence state. The existence of electron transfer can also be confirmed by X-ray absorption near edge structure (XANES). The absorption peak around 11,567 eV can be considered as the electron transition from the 2p to the 5d orbit, and the height of the white line is related to the filling degree of the 5d band for Pt [26,39]. As illustrated in Fig. 2b, the height of white line is in the order of Pt-CNT > Pt-CNT@SnO<sub>2</sub>-400 > Pt-CNT@SnO<sub>2</sub>-200, indicating that the Pt-CNT@SnO<sub>2</sub>-200 and Pt-CNT@SnO<sub>2</sub>-400 have a fuller 5d band filling degree than Pt-CNT.

Numerous studies have demonstrated that the surface strain of Pt-based catalysts is directly linked to their ORR activity [40]. To verify the surface strain of Pt on the CNT@SnO<sub>2</sub> supports, the Pt L<sub>3</sub> K<sup>3</sup>-weight Fourier transform extended X-ray absorption fine structure (FT-EXAFS) was carried out. EXAFS results reveal that the Pt-Pt bond length in Pt-CNT@SnO<sub>2</sub> (2.760 Å) and Pt-CNT@SnO<sub>2</sub> (2.759 Å) is close to that of Pt foil (2.765 Å) (Fig. 2c and Table S1) indicating that the bond length change of Pt-Pt bond is less than 0.2 %. In addition, no obvious strain on Pt lattice is observed in HAADF-STEM. Therefore, the strain effect of Pt induced by SnO<sub>2</sub> can be almost ignored.

The electron transfer between SnO<sub>2</sub> and Pt can be attributed to the difference of their work functions, which is described by the EMSI. To optimize the EMSI between Pt and SnO<sub>2</sub>, the annealing temperature of CNT@SnO<sub>2</sub> was adjusted to tune the oxygen vacancy concentration. Electron paramagnetic resonance (EPR) spectroscopy results (Fig. 2d) suggest that all g-values of Pt-CNT@SnO<sub>2</sub>-T are equal to 2.001, corresponding to the signal of O vacancy [41,42]. With the increase of annealing temperature, the peak at g-value of 2.001 gradually weakens, pointing to the decrease of O vacancy concentration. Valence band XPS

spectra of different Pt-CNT@SnO<sub>2</sub> samples (Fig. 2e), reveal that the d-band center of Pt shifts negatively with the decrease of annealing temperature. For SnO<sub>2</sub>, its work function decreases with the increase of oxygen vacancy concentration [43]. The larger difference of the work function between Pt (5.84 eV) and SnO<sub>2</sub> (~5.1 eV[43,44]) will enhance the charge transfer between them and fill more electrons into the d-band of Pt, resulting in the negative shift of the d-band center of Pt. Interestingly, the d-band center of Pt shows a linear relationship with the oxygen vacancy concentration of SnO<sub>2</sub>, which demonstrates that EMSI between Pt and SnO<sub>2</sub> could be regulated via tuning the oxygen vacancy concentration of SnO<sub>2</sub>. Moreover, comparing to the commercial Pt/C and Pt-CNT (Fig. S7), the Pt-CNT@SnO<sub>2</sub>-400 exhibits ~0.2 eV negative shift of the d-band center of Pt. Previous researches have theoretically and experimentally proved that appropriate drop of d-band center of Pt will result in an optimized adsorption energy for O intermediates [45, 46], which contributes to the improved ORR activity.

### 3.3. Electrochemical performance

Cyclic voltammetry (CV) and linear scanning voltammetry (LSV) were performed in N<sub>2</sub>- and O<sub>2</sub>- saturated 0.1 M HClO<sub>4</sub> to investigate the ORR performance of the developed catalysts. The electrochemically active surface areas (ECSAs) of the catalysts are calculated to be 57.7, 51.4, and 48.58 m<sup>2</sup> g<sub>Pt</sub><sup>-1</sup> for commercial Pt/C, Pt-CNT, and Pt-CNT@SnO<sub>2</sub>-400, respectively. These catalysts reveal similar ECSAs, but the CV curve of Pt-CNT@SnO<sub>2</sub>-400 shows unique characteristics (Fig. 3a and Fig. S8). In the region corresponding to the Pt redox, the Pt-CNT@SnO<sub>2</sub>-400 reveals a smaller current density than that of Pt/C and Pt-CNT, which mean that the introduction of SnO<sub>2</sub> can retard the formation of oxidized Pt species [47]. This phenomenon further verifies the EMSI between Pt and SnO<sub>2</sub>. From LSV, the Pt-CNT@SnO<sub>2</sub>-400 sample exhibits a higher ORR activity with half-wave potential (*E*<sub>1/2</sub>) of 0.887 V vs. RHE (Fig. 3b), compared to commercial Pt/C (0.863 V) and Pt-CNT (0.851 V). The *E*<sub>1/2</sub> and ECSA of other samples are summarized in Supplementary Table 2.

As discussed above, regulating the EMSI between Pt and SnO<sub>2</sub> reduces the d-band center of Pt. Pt-CNT@SnO<sub>2</sub>-400 also exhibits the highest ORR activity with the most positive half-wave potential (*E*<sub>1/2</sub> = 0.887 V vs. RHE) than other Pt-CNT@SnO<sub>2</sub> catalysts (0.870 V, 0.836 V, 0.801 V and 0.789 V for Pt-CNT@SnO<sub>2</sub>-300, Pt-CNT@SnO<sub>2</sub>-200, Pt-CNT@SnO<sub>2</sub>-500 and Pt-CNT@SnO<sub>2</sub>, respectively) from the ORR polarization curves (Fig. 3c and Table S3). Further, we find a volcanic relationship between the ORR activity of the catalysts and their d-band center (Fig. 3d). With the decrease of d-band center of Pt-CNT@SnO<sub>2</sub>, and the catalytic activity increases first and then decreases. The volcanic relationship suggests that the ORR activity can be regulated by tuning the d-band center of Pt through tailoring the electron transfer between Pt and CNT@SnO<sub>2</sub>.

We screened the developed catalysts in MEA for practical PEMFC applications. It needs to emphasize that the added amount of ionomer should be carefully optimized due to the surface area, hydrophobicity of supports, and the coverage of Pt on the surface of Pt-CNT@SnO<sub>2</sub>-400 are quite different from that of commercial Pt/C (Figs. S9–S10). The fuel cell polarization curves (i–V) of the commercial Pt/C and Pt-CNT@SnO<sub>2</sub>-400 are shown in Fig. 3e–f. The maximum power density of Pt-CNT@SnO<sub>2</sub>-400 is 1618 mW cm<sup>-2</sup> under the H<sub>2</sub>-O<sub>2</sub> condition with cathode Pt loading of 0.096 mg cm<sup>-2</sup>, and the MA at 0.9 V<sub>ir-free</sub> is 0.68 A mg<sub>Pt</sub><sup>-1</sup>, which exceeds the U.S DOE 2025 target (0.44 A mg<sub>Pt</sub><sup>-1</sup>) and is much improved over commercial Pt/C (0.11 A mg<sub>Pt</sub><sup>-1</sup>). Noteworthy, the Pt-CNT@SnO<sub>2</sub>-400 exhibits remarkable performance in the kinetic region (256 mA cm<sup>-2</sup> @ 0.8 V) under the H<sub>2</sub>-Air condition, while the kinetic current at 0.8 V of commercial Pt/C is only 116 mA cm<sup>-2</sup>. Our Pt-CNT@SnO<sub>2</sub>-400 exhibits higher activity in MEA compare to other pure-Pt-based ORR catalysts (Table S3).

Under the fuel cell start-stop or load-change conditions, the cathode catalyst will endure high voltage of ~1.5 V, which poses severe

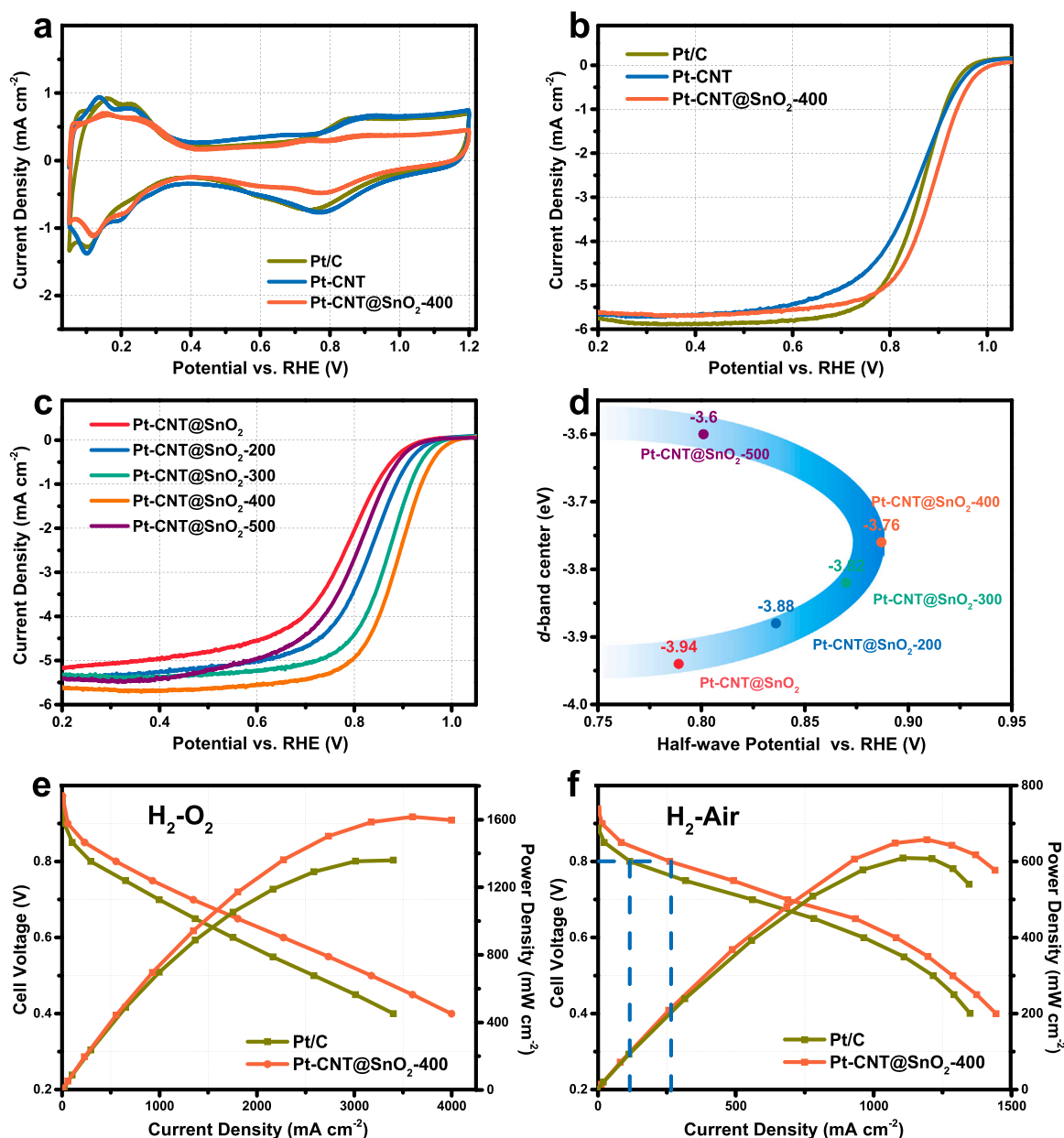


**Fig. 3.** (a) CV curves of Pt/C, Pt-CNT and Pt-CNT@SnO<sub>2</sub>-400 in N<sub>2</sub>-saturated 0.1 M HClO<sub>4</sub> (scan rate, 50 mV s<sup>-1</sup>). (b) ORR polarization curves of Pt/C, Pt-CNT and Pt-CNT@SnO<sub>2</sub>-400 in O<sub>2</sub>-saturated 0.1 M HClO<sub>4</sub> (rotating speed, 1600 rpm; scan rate, 10 mV s<sup>-1</sup>). (c) ORR polarization curves of Pt-CNT@SnO<sub>2</sub>-T (T = 0, 200, 300, 400 and 500) in O<sub>2</sub>-saturated 0.1 M HClO<sub>4</sub> (rotating speed, 1600 rpm; scan rate, 10 mV s<sup>-1</sup>). (d) The relationship between *d*-band center of Pt and the ORR activity of catalysts. (e) H<sub>2</sub>-O<sub>2</sub> fuel cell and (f) H<sub>2</sub>-Air fuel cell polarization curves of commercial Pt/C and Pt-CNT@SnO<sub>2</sub>-400.

corrosion challenges for carbon supports. However, conventional accelerated durability testing (ADT) at 0.6–0.95 V is used to evaluate the stability of metal NPs [48], which avoids the higher potential region where the corrosion of carbon carrier usually occurs. To examine the stability of the catalyst more rigorously, the electrochemical stability of the catalysts was investigated at a high potential region between 1.0 and 1.6 V, as suggested by U.S. DOE. After 50,000 cycles of high potential stability testing, Pt-CNT@SnO<sub>2</sub>-400 maintains a high activity and displays only 11 mV shift of *E*<sub>1/2</sub>, while the *E*<sub>1/2</sub> of Pt-CNT lost 78 mV with only 30,000 cycles (Fig. 4a). After 50,000 ADT cycles, the MA of Pt-CNT@SnO<sub>2</sub>-400 at 0.9 V is decreased by 20.5 % from 0.29 A mg<sub>Pt</sub><sup>-1</sup>, while the surface activity (SA) is decreased by 10.3 % from 0.60 mA cm<sup>-2</sup> (Fig. 4c). In the contrast, the MA and SA of Pt-CNT are decreased by 68.8 % and 31.8 %, respectively, after only 30,000 cycles. In addition, the ECSA of Pt-CNT@SnO<sub>2</sub>-400 only decreases by 11.3 %

after 50,000 cycles (Fig. 4b). Compared to all the Pt-based catalysts reported so far, our Pt-CNT@SnO<sub>2</sub>-400 catalyst exhibits the best durability under the high potential ADT conditions (Fig. 4d) [19,20,26,49, 50]. In the contrast, Pt-CNT suffers from the 46.6 % ECSA loss of Pt after 30,000 cycles.

In fuel cells, the Pt-CNT@SnO<sub>2</sub>-400 catalyst also demonstrates immense stability improvement compared to commercial Pt/C. After 5000 cycles ADT from 1.0 to 1.5 V, the i-V curve of Pt-CNT@SnO<sub>2</sub>-400 shows negligible change with only 9.2 % MA loss at 0.9 V<sub>IR-free</sub> (Fig. 4e), exceeding the U.S. DOE 2025 target (<40 % MA loss after 5000 cycles). In the contrast, commercial Pt/C is almost inactivated after ADT and the MA at 0.9 V<sub>IR-free</sub> cannot be collected, which could be attributed to the structural collapse caused by the oxidative corrosion of the carbon support and the water flooding of the catalyst layer due to the increase of hydrophilicity. Furthermore, the loss of power density could directly

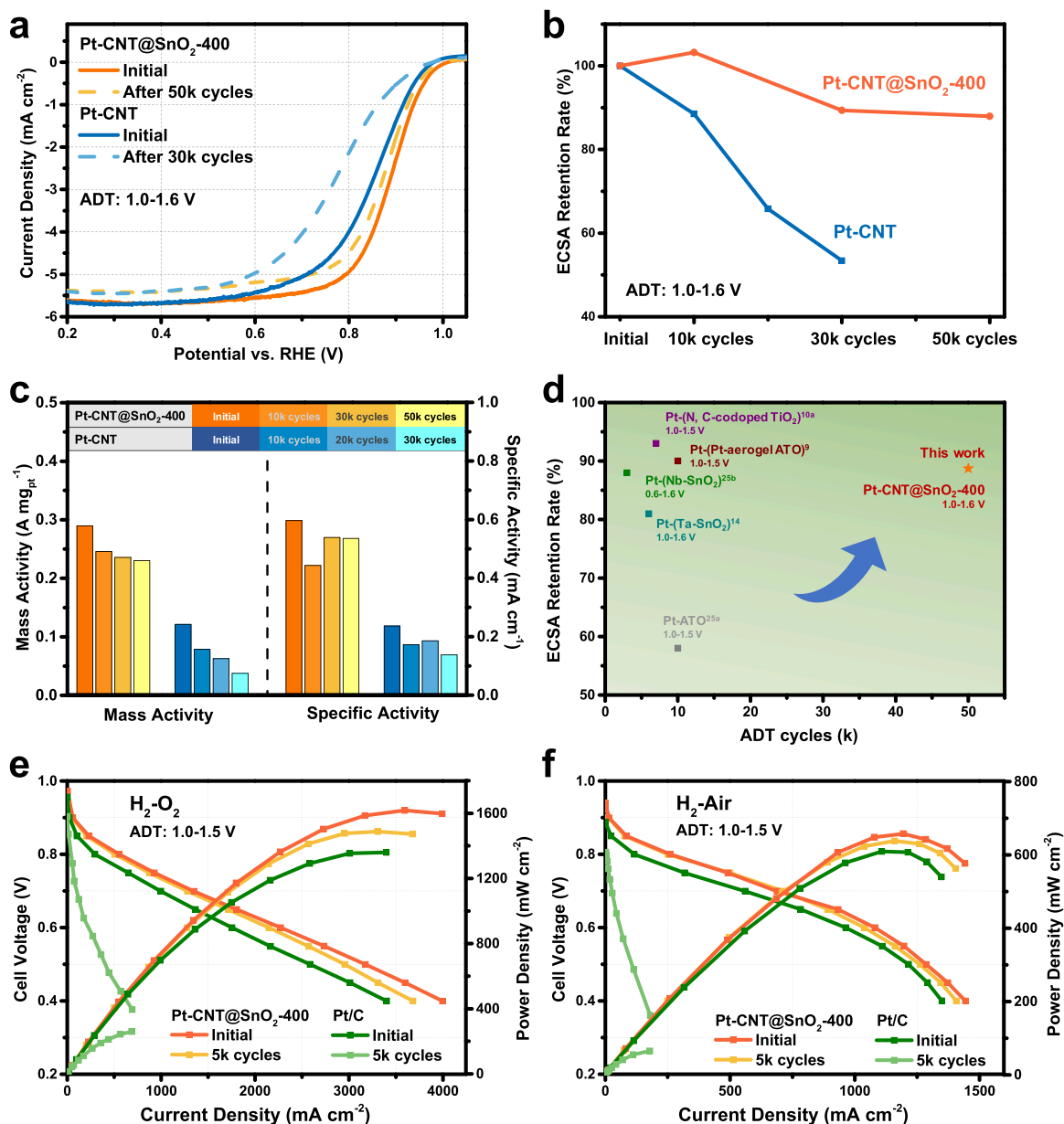


**Fig. 4.** ORR polarization curves of (a) Pt-CNT@SnO<sub>2</sub>-400 and Pt-C in O<sub>2</sub>-saturated 0.1 M HClO<sub>4</sub> before and after ADT (rotating speed, 1600 rpm; scan rate, 10 mV s<sup>-1</sup>. ADT test: 1.0–1.6 V). (b) The ECSA retention of Pt-CNT@SnO<sub>2</sub>-400 and Pt-CNT during ADT. (c) MA and SA of Pt-CNT@SnO<sub>2</sub>-400 at 0.9 V during ADT. (d) Comparison of the ECSA retention for oxide-based support catalysts between this work and previous work. (e) H<sub>2</sub>-O<sub>2</sub> fuel cell polarization curves of Pt-CNT@SnO<sub>2</sub>-400 and commercial Pt/C after 5k cycles ADT. (f) H<sub>2</sub>-Air fuel cell polarization curves of Pt-CNT@SnO<sub>2</sub>-400 and commercial Pt/C after 5k cycles ADT.

reflect the collapse of the catalyst layer. The power densities of Pt-CNT@SnO<sub>2</sub>-400 merely loss 8 % and 3 % in H<sub>2</sub>-O<sub>2</sub> in H<sub>2</sub>-air modes (Fig. 4f), respectively, significantly outperforming that of the commercial Pt/C (81 % and 89 % losses). The remarkably improved durability of the developed catalyst compared to Pt/C demonstrate that the successful design of SnO<sub>2</sub>-coated CNTs structure and the strong bonding interaction between Pt and SnO<sub>2</sub>.

### 3.4. Mechanism analysis

The activity loss caused by supports corrosion should be taken seriously. We infer that the design of the cable structure could inhibit carbon corrosion. To verify our hypothesis, the gas products produced by the Pt-C, Pt-CNT, Pt-CNT@SnO<sub>2</sub>-400 at 1.6 V were analyzed by gas chromatography (GC) [51]. Under the high potential, the carbon corrosion cannot be ignored, and the current-time (i-t) curve of carbon corrosion is

recorded in Fig. 5a. The minimum normalized current density indicates that the CO<sub>2</sub> corrosion of Pt-CNT@SnO<sub>2</sub>-400 is much weaker than that of Pt/C and Pt-CNT. After fully purifying the electrolytic cell with Ar gas, the products generated by the corrosion of the Pt-C, Pt-CNT, Pt-CNT@SnO<sub>2</sub>-400 are collected and analyzed by GC. As shown in Fig. 5b, the commercial Pt/C generates most CO<sub>2</sub>, about ~110 ppm mg<sub>C</sub><sup>-1</sup>, while the Pt-CNT with high graphitization degree produces less CO<sub>2</sub>, about ~80 ppm mg<sub>C</sub><sup>-1</sup>. Noteworthy, the Pt-CNT@SnO<sub>2</sub>-400 produces the least CO<sub>2</sub> yield among the studied samples (~10 ppm mg<sub>C</sub><sup>-1</sup>), which provides a solid evidence that SnO<sub>2</sub> coating could effectively protect the carbon from corrosion. The durable support results in less Pt dissolution after ADT in high potential region. The ICP-OES tests (Table S4) for the electrolyte after 10k cycles ADT (1.0–1.6 V) manifest that only ~0.7 wt% Pt and ~0.06 wt% Sn in Pt-CNT@SnO<sub>2</sub>-400 dissolve, while ~2.3 wt% Pt in the commercial Pt/C dissolves.

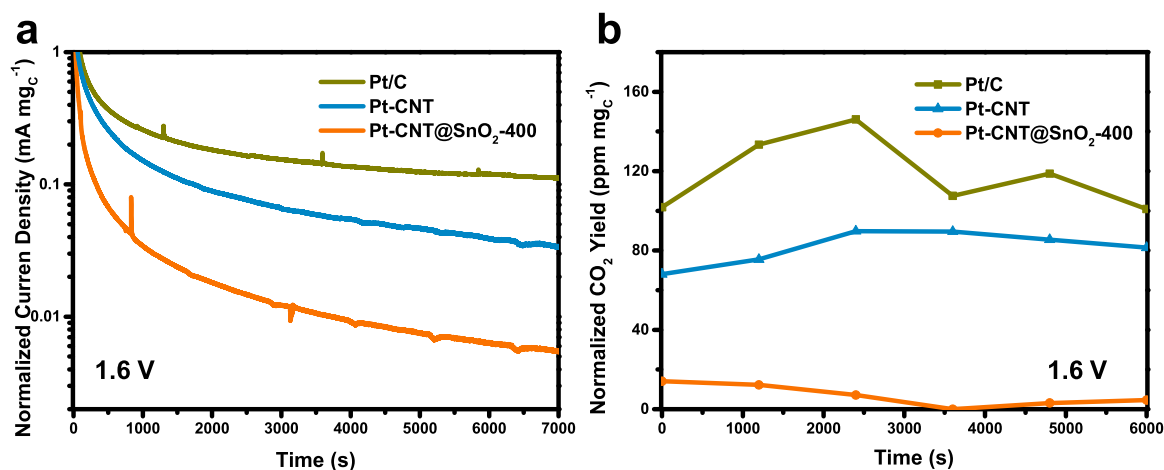


Fig. 5. (a) The normalized current-time curve of Pt-C, Pt-CNT, and Pt-CNT@SnO<sub>2</sub>-400 in Ar-saturated 0.1 M HClO<sub>4</sub> at 1.6 V. (b) The normalized CO<sub>2</sub> yields of Pt-C, Pt-CNT, and Pt-CNT@SnO<sub>2</sub>-400.

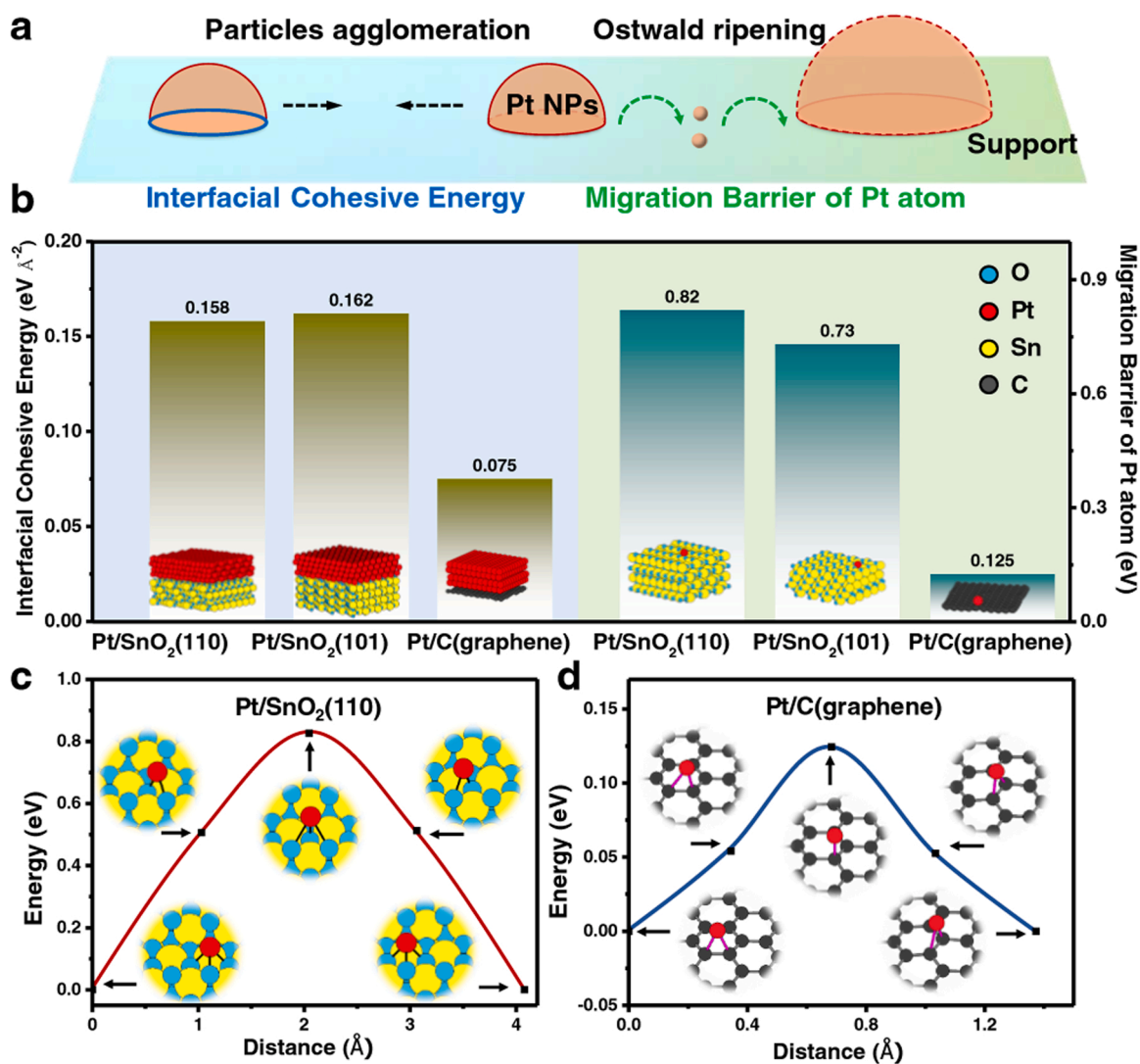


Fig. 6. (a) Schematic illustration for the particle agglomeration and Ostwald ripening processes. (b) The left panel compares the interfacial cohesive energies of Pt/SnO<sub>2</sub>(110), Pt/SnO<sub>2</sub>(101) and Pt/graphene, while the right panel compares the energy barriers of a Pt atom migrating on the surfaces of SnO<sub>2</sub>(110), SnO<sub>2</sub>(101) and graphene. The migration pathways and energy barriers determined from the DFT-NEB calculations are shown in (c) and (d) for Pt migration on SnO<sub>2</sub>(110) and C(graphene) surfaces, respectively.



In addition, the growth of Pt particles also leads to loss of activity, which could contribute to the agglomeration of Pt nanoparticles and Ostwald ripening (Fig. 6a). As a comparison, the average sizes of Pt particles on Pt-CNT@SnO<sub>2</sub>-400 and Pt/C increase to ~4.05 nm and ~6.49 nm, respectively, after ADT under high potential (Fig. S11). Meanwhile, the EPR measurements of Pt-CNT@SnO<sub>2</sub>-400 after activation and ADT (Fig. S12) demonstrate that the concentration of oxygen vacancy in SnO<sub>2</sub> is almost unchanged during the potential cycling.

DFT calculations were carried out to understand the SMSBI and mechanism of durability enhancement. The computational models are displayed in Figs. S13–S14, and all of them were fully optimized to make Pt strain-free. To assess the interfacial stability, we calculate the interfacial cohesive energies for Pt/SnO<sub>2</sub> and Pt/graphene. As shown in the left panel of Fig. 5b, the interfacial cohesive energy for Pt/SnO<sub>2</sub>(110) is 0.158 eV Å<sup>-2</sup> and Pt/SnO<sub>2</sub>(101) is 0.162 eV Å<sup>-2</sup>, both are much stronger than that of Pt/graphene (0.075 eV Å<sup>-2</sup>). The stronger interfacial cohesive energy indicates that Pt particles are anchored more firmly on the SnO<sub>2</sub> surfaces than on graphene, which in turn implies that the agglomeration of Pt particles on the SnO<sub>2</sub> surfaces is unlikely [27]. As shown on the right panel of Fig. 6b, c and d, the energy barriers of a Pt atom migrating on the SnO<sub>2</sub> surfaces are about 5 times higher than that on graphene, suggesting that Pt migration on the SnO<sub>2</sub> surfaces is much suppressed compared on graphene. Therefore, the growth of Pt particles via Ostwald ripening is expected to be attenuated by the strong interaction between Pt and SnO<sub>2</sub>.

#### 4. Conclusions

In summary, cable-like core@shell CNTs@SnO<sub>2</sub> was successfully developed as advanced supports for Pt particles as ORR catalysts with unprecedented electrochemical stability. SnO<sub>2</sub> could serve as a protection layer of CNTs against corrosion and stabilize Pt NPs in the operating conditions of a PEMFC. Meanwhile, comprehensive physical characterizations prove that the EMSI between Pt and SnO<sub>2</sub> could induce a favorable downshift of Pt *d*-band center. The PEMFC tests demonstrate that the Pt-CNT@SnO<sub>2</sub>-400 cathode displays extraordinarily high activity, with MA of 0.68 A mg<sub>Pt</sub><sup>-1</sup> and peak power density of 1618 mW cm<sup>-2</sup>, compared to Pt-CNT and Pt/C. Importantly, Pt-CNT@SnO<sub>2</sub>-400 demonstrates the best stability ever reported after ADT in electrochemical half-cells under high potential region (1.0–1.6 V), with a record-low ECSA loss of 11.3 % (after 50,000 cycles) and a much reduced CO<sub>2</sub> yield, while the ADT in MEA (1.0–1.5 V) only cause 9.2 % MA and 8 % power density loss after 5k cycles. DFT calculations indicate that the SMSBI between Pt and SnO<sub>2</sub> enables stronger interfacial cohesion and greater migration barriers for Pt atoms on the SnO<sub>2</sub> surfaces, relative to carbon, which are responsible for the impressive durability of the catalysts observed in the experiments. This work highlights the significant importance of rationally tuning metal-support interactions towards the improvement of the electrocatalytic activity and durability for energy conversion technologies.

#### CRediT authorship contribution statement

**Shenzhou Li:** Investigation, Conceptualization, Data curation, Formal analysis, Methodology, Validation, Writing - original draft. **Junyi Liu:** Conceptualization, Methodology, Writing - review & editing. **Jiashun Liang:** Validation, Investigation. **Zijie Lin:** Validation, Investigation. **Xuan Liu:** Validation, Investigation. **Yuan Chen:** Methodology, Resources. **Gang Lu:** Conceptualization, Methodology, Writing - review & editing. **Chengliang Wang:** Methodology, Resources. **Peng Wei:** Methodology, Resources. **Jiantao Han:** Methodology, Resources. **Yunhui Huang:** Resources, Writing - review & editing. **Gang Wu:** Resources, Writing - review & editing. **Qing Li:** Conceptualization, Methodology, Investigation, Resources, Writing - review & editing, Supervision, Project administration.

#### Declaration of Competing Interest

The authors declare that they have no known competing financial interests or personal relationships that could have appeared to influence the work reported in this paper.

#### Data availability

All data are available in the main text or the [supplementary materials](#).

#### Acknowledgements

This work was financially supported by National Natural Science Foundation of China (22122202, 21972051). The work at California State University Northridge was supported by the US NSF-PREM Program (DMR-1828019). The authors thank the Analytical and Testing Center of Huazhong University of Science and Technology (HUST) for carrying out the XPS, SEM, and TEM measurements. The authors thank BL11B in Shanghai Synchrotron Radiation Facility (SSRF) for providing the beam time.

#### Appendix A. Supporting information

Supplementary data associated with this article can be found in the online version at [doi:10.1016/j.apcatb.2022.122017](https://doi.org/10.1016/j.apcatb.2022.122017).

#### References

- [1] D.A. Cullen, K.C. Neyerlin, R.K. Ahluwalia, R. Mukundan, K.L. More, R.L. Borup, A. Z. Weber, D.J. Myers, A. Kusoglu, New roads and challenges for fuel cells in heavy-duty transportation, *Nat. Energy* 6 (2021) 462–474, <https://doi.org/10.1038/s41560-021-00775-z>.
- [2] M.K. Debe, Electrocatalyst approaches and challenges for automotive fuel cells, *Nature* 486 (2012) 43–51, <https://doi.org/10.1038/nature11115>.
- [3] J. Liang, X. Liu, Q. Li, Principles, strategies, and approaches for designing highly durable platinum-based catalysts for proton exchange membrane fuel cells, *Acta Phys. Chim. Sin.* 37 (2021), <https://doi.org/10.3866/pku.Whxb202010072>.
- [4] J. Fan, M. Chen, Z. Zhao, Z. Zhang, S. Ye, S. Xu, H. Wang, H. Li, Bridging the gap between highly active oxygen reduction reaction catalysts and effective catalyst layers for proton exchange membrane fuel cells, *Nat. Energy* 6 (2021) 475–486, <https://doi.org/10.1038/s41560-021-00824-7>.
- [5] J.C. Meier, C. Galeano, I. Katsounaros, A.A. Topalov, A. Kostka, F. Schüth, K.J. J. Mayrhofer, Degradation mechanisms of Pt/C fuel cell catalysts under simulated start-stop conditions, *ACS Catal.* 2 (2012) 832–843, <https://doi.org/10.1021/cs300024h>.
- [6] S. Cherevko, N. Kulyk, K.J.J. Mayrhofer, Durability of platinum-based fuel cell electrocatalysts: dissolution of bulk and nanoscale platinum, *Nano Energy* 29 (2016) 275–298, <https://doi.org/10.1016/j.nanoen.2016.03.005>.
- [7] J. Zhang, Y. Yuan, L. Gao, G. Zeng, M. Li, H. Huang, Stabilizing Pt-based electrocatalysts for oxygen reduction reaction: fundamental understanding and design strategies, *Adv. Mater.* 33 (2021), 2006494, <https://doi.org/10.1002/adma.202006494>.
- [8] C.A. Reiser, L. Bregoli, T.W. Patterson, J.S. Yi, J.D.L. Yang, M.L. Perry, T.D. Jarvi, A reverse-current decay mechanism for fuel cells, *Electrochem. Solid State Lett.* 8 (2005) A273–A276, <https://doi.org/10.1149/1.1896466>.
- [9] S.-M. Jung, S.-W. Yun, J.-H. Kim, S.-H. You, J. Park, S. Lee, S.H. Chang, S.C. Chae, S.H. Joo, Y. Jung, J. Lee, J. Son, J. Snyder, V. Stamenkovic, N.M. Markovic, Y.-T. Kim, Selective electrocatalysis imparted by metal-insulator transition for durability enhancement of automotive fuel cells, *Nat. Catal.* 3 (2020) 639–648, <https://doi.org/10.1038/s41929-020-0475-4>.
- [10] H. Schulenburg, B. Schwanitz, N. Linse, G.G. Scherer, A. Wokaun, J. Krbanjevic, R. Grothausmann, I. Manke, 3D imaging of catalyst support corrosion in polymer electrolyte fuel cells, *J. Phys. Chem. C* 115 (2011) 14236–14243, <https://doi.org/10.1021/jp203016u>.
- [11] Z. Qiao, S. Hwang, X. Li, C. Wang, W. Samarakoon, S. Karakalos, D. Li, M. Chen, Y. He, M. Wang, Z. Liu, G. Wang, H. Zhou, Z. Feng, D. Su, J.S. Spendlow, G. Wu, 3D porous graphitic nanocarbon for enhancing the performance and durability of Pt catalysts: a balance between graphitization and hierarchical porosity, *Energy Environ. Sci.* 12 (2019) 2830–2841, <https://doi.org/10.1039/c9ee01899a>.
- [12] Y.-J. Wang, B. Fang, H. Li, X.T. Bi, H. Wang, Progress in modified carbon support materials for Pt and Pt-alloy cathode catalysts in polymer electrolyte membrane fuel cells, *Prog. Mater. Sci.* 82 (2016) 445–498, <https://doi.org/10.1016/j.pmatsci.2016.06.002>.
- [13] D. Gohl, A. Garg, P. Paciok, K.J.J. Mayrhofer, M. Heggen, Y. Shao-Horn, R. E. Dunin-Borkowski, Y. Roman-Leshkov, M. Ledendecker, Engineering stable

- electrocatalysts by synergistic stabilization between carbide cores and Pt shells, *Nat. Mater.* 19 (2020) 287–291, <https://doi.org/10.1038/s41563-019-0555-5>.
- [14] C. Xu, C. Fan, X. Zhang, H. Chen, X. Liu, Z. Fu, R. Wang, T. Hong, J. Cheng, MXene (Ti<sub>3</sub>C<sub>2</sub>Tx) and carbon nanotube hybrid-supported platinum catalysts for the high-performance oxygen reduction reaction in PEMFC, *ACS Appl. Mater. Interfaces* 12 (2020) 19539–19546, <https://doi.org/10.1021/acsami.0c02446>.
  - [15] N. Cheng, M.N. Banis, J. Liu, A. Riese, S. Mu, R. Li, T.-K. Sham, X. Sun, Atomic scale enhancement of metal-support interactions between Pt and ZrC for highly stable electrocatalysts, *Energy Environ. Sci.* 8 (2015) 1450–1455, <https://doi.org/10.1039/c4ee04086d>.
  - [16] Y. Xiao, G. Zhan, Z. Fu, Z. Pan, C. Xiao, S. Wu, C. Chen, G. Hu, Z. Wei, Titanium cobalt nitride supported platinum catalyst with high activity and stability for oxygen reduction reaction, *J. Power Sources* 284 (2015) 296–304, <https://doi.org/10.1016/j.jpowsour.2015.03.001>.
  - [17] H. Shintani, K. Kakinuma, H. Uchida, M. Watanabe, M. Uchida, Performance of practical-sized membrane-electrode assemblies using titanium nitride-supported platinum catalysts mixed with acetylene black as the cathode catalyst layer, *Chem. Sci.* 280 (2015) 593–599, <https://doi.org/10.1016/j.jpowsour.2015.01.132>.
  - [18] M.A. Abdelkareem, T. Wilberforce, K. Elsaid, E.T. Sayed, E.A.M. Abdelghani, A. G. Olabi, Transition metal carbides and nitrides as oxygen reduction reaction catalyst or catalyst support in proton exchange membrane fuel cells (PEMFCs), *Int. J. Hydrog. Energy* 46 (2021) 23529–23547, <https://doi.org/10.1016/j.ijhydene.2020.08.250>.
  - [19] I. Jiménez-Morales, F. Haidar, S. Cavaliere, D. Jones, J. Rozière, Strong interaction between platinum nanoparticles and tantalum-doped tin oxide nanofibers and its activation and stabilization effects for oxygen reduction reaction, *ACS Catal.* 10 (2020) 10399–10411, <https://doi.org/10.1021/acscatal.0c02220>.
  - [20] E. Lee, C. Park, D.W. Lee, G. Lee, H.-Y. Park, J.H. Jang, H.-J. Kim, Y.-E. Sung, Y. Tak, S.-J. Yoo, Tunable synthesis of N,C-codoped Ti<sub>3</sub>C<sub>2</sub>-enriched titanium oxide support for highly durable PEMFC cathode, *ACS Catal.* 10 (2020) 12080–12090, <https://doi.org/10.1021/acscatal.0c02570>.
  - [21] V.T. Ho, C.J. Pan, J. Rick, W.N. Su, B.J. Hwang, Nanostructured Ti(0.7)Mo(0.3)O<sub>2</sub> support enhances electron transfer to Pt: high-performance catalyst for oxygen reduction reaction, *J. Am. Chem. Soc.* 133 (2011) 11716–11724, <https://doi.org/10.1021/ja2039562>.
  - [22] N.C. Cheng, M.N. Banis, J. Liu, A. Riese, X. Li, R.Y. Li, S.Y. Ye, S. Knights, X.L. Sun, Extremely stable platinum nanoparticles encapsulated in a zirconia nanocage by area-selective atomic layer deposition for the oxygen reduction reaction, *Adv. Mater.* 27 (2015) 277–281, <https://doi.org/10.1002/adma.201404314>.
  - [23] Y. Takabatake, Z. Noda, S.M. Lyth, A. Hayashi, K. Sasaki, Cycle durability of metal oxide supports for PEFC electrocatalysts, *Int. J. Hydrog. Energy* 39 (2014) 5074–5082, <https://doi.org/10.1016/j.ijhydene.2014.01.094>.
  - [24] R. Lang, W. Xi, J.C. Liu, Y.T. Cui, T. Li, A.F. Lee, F. Chen, Y. Chen, L. Li, L. Li, J. Lin, S. Miao, X. Liu, A.Q. Wang, X. Wang, J. Luo, B. Qiao, J. Li, T. Zhang, Non defect-stabilized thermally stable single-atom catalyst, *Nat. Commun.* 10 (2019) 234, <https://doi.org/10.1038/s41467-018-08136-3>.
  - [25] M. Eckardt, C. Gebauer, Z. Jusys, M. Wassner, N. Hüsing, R.J. Behm, Oxygen reduction reaction activity and long-term stability of platinum nanoparticles supported on titania and titania-carbon nanotube composites, *J. Power Sources* 400 (2018) 580–591, <https://doi.org/10.1016/j.jpowsour.2018.08.036>.
  - [26] C. He, S. Sankarasubramanian, A. Ellis, J. Parrondo, C. Gumei, M. Kodali, I. Matanovic, A.K. Yadav, K. Bhattacharyya, N. Dale, P. Atanassov, V.K. Ramani, Self-anchored platinum-decorated antimony-doped-tin oxide as a durable oxygen reduction electrocatalyst, *ACS Catal.* 11 (2021) 7006–7017, <https://doi.org/10.1021/acscatal.1c00963>.
  - [27] S. Hu, W.-X. Li, Sabatier principle of metal-support interaction for design of ultrastable metal nanocatalysts, *Science* 374 (2021) 1360–1365, <https://doi.org/10.1126/science.abi9828>.
  - [28] G. Kresse, J. Furthmüller, Efficient iterative schemes for ab initio total-energy calculations using a plane-wave basis set, *Phys. Rev. B* 54 (1996) 11169.
  - [29] P.E. Blöchl, Projector augmented-wave method, *Phys. Rev. B* 50 (1994) 17953.
  - [30] J.P. Perdew, K. Burke, M. Ernzerhof, Generalized gradient approximation made simple, *Phys. Rev. Lett.* 77 (1996) 3865.
  - [31] H.J. Monkhorst, J.D. Pack, Special points for Brillouin-zone integrations, *Phys. Rev. B* 13 (1976) 5188–5192, <https://doi.org/10.1103/PhysRevB.13.5188>.
  - [32] G. Henkelman, B.P. Uberuaga, H. Jónsson, A climbing image nudged elastic band method for finding saddle points and minimum energy paths, *J. Chem. Phys.* 113 (2000) 9901–9904, <https://doi.org/10.1063/1.1329672>.
  - [33] G. Henkelman, H. Jónsson, Improved tangent estimate in the nudged elastic band method for finding minimum energy paths and saddle points, *J. Chem. Phys.* 113 (2000) 9978–9985, <https://doi.org/10.1063/1.1323224>.
  - [34] S. Grimme, Semiempirical GGA-type density functional constructed with a long-range dispersion correction, *J. Comput. Chem.* 27 (2006) 1787–1799.
  - [35] F. Luo, S. Liao, D. Dang, Y. Zheng, D. Xu, H. Nan, T. Shu, Z. Fu, Tin and silicon binary oxide on the carbon support of a Pt electrocatalyst with enhanced activity and durability, *ACS Catal.* 5 (2015) 2242–2249, <https://doi.org/10.1021/cs501429g>.
  - [36] N. Zhang, S. Zhang, C. Du, Z. Wang, Y. Shao, F. Kong, Y. Lin, G. Yin, Pt/Tin oxide/carbon nanocomposites as promising oxygen reduction electrocatalyst with improved stability and activity, *Electrochim. Acta* 117 (2014) 413–419, <https://doi.org/10.1016/j.electacta.2013.11.139>.
  - [37] J. Guan, Y. Zan, R. Shao, J. Niu, M. Dou, B. Zhu, Z. Zhang, F. Wang, Phase segregated Pt-SnO<sub>2</sub>/C nanohybrids for highly efficient oxygen reduction electrocatalysis, *Small* 16 (2020), 2005048, <https://doi.org/10.1002/smll.202005048>.
  - [38] Y. Chino, K. Taniguchi, Y. Senoo, K. Kakinuma, M. Hara, M. Watanabe, M. Uchida, Effect of added graphitized CB on both performance and durability of Pt/Nb-SnO<sub>2</sub> cathodes for PEFCs, *J. Electrochem. Soc.* 162 (2015) F736–F743, <https://doi.org/10.1149/2.0651507jes>.
  - [39] X. Wu, Q. Li, X. Wang, Z. Xie, X. Yang, X. Yu, X. Zhang, Z. Lu, L. Li, Pd nanoparticles loaded on TiO<sub>2</sub>-C heterostructure via photochemical strategy for efficient oxygen reduction reaction, *New J. Chem.* 45 (2021) 18379–18386, <https://doi.org/10.1039/d1nj02718b>.
  - [40] J. Liang, Z. Zhao, N. Li, X. Wang, S. Li, X. Liu, T. Wang, G. Lu, D. Wang, B. J. Hwang, Y. Huang, D. Su, Q. Li, Biaxial strains mediated oxygen reduction electrocatalysis on fenton reaction resistant L1<sub>0</sub>-PtZn fuel cell cathode, *Adv. Energy Mater.* 10 (2020), 2000179, <https://doi.org/10.1002/aenm.202000179>.
  - [41] C. Drouilly, J.-M. Krafft, F. Averseng, S. Casale, D. Bazer-Bachi, C. Chizallet, V. Lecocq, H. Vezin, H. Lauro-Pernot, G. Costentin, ZnO oxygen vacancies formation and filling followed by in situ photoluminescence and in situ EPR, *J. Phys. Chem. C* 116 (2012) 21297–21307, <https://doi.org/10.1021/jp307693y>.
  - [42] B.L. Yu, C.S. Zhu, F.X. Gan, Y.B. Huang, Electron spin resonance properties of ZnO microcrystallites, *Mater. Lett.* 33 (1998) 247–250, [https://doi.org/10.1016/s0167-577x\(97\)00117-1](https://doi.org/10.1016/s0167-577x(97)00117-1).
  - [43] T.C. Yeh, Q. Zhu, D.B. Buchholz, A.B. Martinson, R.P.H. Chang, T.O. Mason, Amorphous transparent conducting oxides in context: work function survey, trends, and facile modification, *Appl. Surf. Sci.* 330 (2015) 405–410, <https://doi.org/10.1016/j.apsusc.2015.01.026>.
  - [44] K.J. Rietwyk, D.A. Keller, A. Ginsburg, H.N. Barad, M. Priel, K. Majhi, Z. Yan, S. Tirosh, A.Y. Anderson, L. Ley, A. Zaban, Universal work function of metal oxides exposed to air, *Adv. Mater. Interfaces* 6 (2019), <https://doi.org/10.1002/admi.201802058>.
  - [45] F. Ando, T. Gunji, T. Tanabe, I. Fukano, H.D. Abruña, J. Wu, T. Ohsaka, F. Matsumoto, Enhancement of the oxygen reduction reaction activity of Pt by tuning its d-Band center via transition metal oxide support interactions, *ACS Catal.* 11 (2021) 9317–9332, <https://doi.org/10.1021/acscatal.1c01868>.
  - [46] J.K. Norskov, J. Rossmeisl, A. Logadottir, L. Lindqvist, J.R. Kitchin, T. Bligaard, H. Jónsson, Origin of the overpotential for oxygen reduction at a fuel-cell cathode, *J. Phys. Chem. B* 108 (2004) 17886–17892, <https://doi.org/10.1021/jp047349j>.
  - [47] W. Gao, Z. Zhang, M. Dou, F. Wang, Highly dispersed and crystalline Ta<sub>2</sub>O<sub>5</sub> anchored Pt electrocatalyst with improved activity and durability toward oxygen reduction: promotion by atomic-scale Pt-Ta<sub>2</sub>O<sub>5</sub> interactions, *ACS Catal.* 9 (2019) 3278–3288, <https://doi.org/10.1021/acscatal.8b04505>.
  - [48] J. Liang, N. Li, Z. Zhao, L. Ma, X. Wang, S. Li, X. Liu, T. Wang, Y. Du, G. Lu, J. Han, Y. Huang, D. Su, Q. Li, Tungsten-doped L1<sub>0</sub>-PtCo ultrasmall nanoparticles as a high-performance fuel cell cathode, *Angew. Chem. Int. Ed.* 58 (2019) 15471–15477, <https://doi.org/10.1002/anie.201908824>.
  - [49] G. Cognard, G. Ozouf, C. Beauger, G. Berthomé, D. Riassetto, L. Dubau, R. Chattot, M. Chatenet, F. Maillard, Benefits and limitations of Pt nanoparticles supported on highly porous antimony-doped tin dioxide aerogel as alternative cathode material for proton-exchange membrane fuel cells, *Appl. Catal., B* 201 (2017) 381–390, <https://doi.org/10.1016/j.apcatb.2016.08.010>.
  - [50] G. Shi, T. Tano, D.A. Tryk, A. Iiyama, M. Uchida, K. Kakinuma, Temperature dependence of oxygen reduction activity at Pt/Nb-doped SnO<sub>2</sub> catalysts with varied Pt loading, *ACS Catal.* 11 (2021) 5222–5230, <https://doi.org/10.1021/acscatal.0c05157>.
  - [51] M. Dou, M. Hou, D. Liang, W. Lu, Z. Shao, B. Yi, SnO<sub>2</sub> nanocluster supported Pt catalyst with high stability for proton exchange membrane fuel cells, *Electrochim. Acta* 92 (2013) 468–473, <https://doi.org/10.1016/j.electacta.2013.01.070>.